Nanoscale
Advances

ROYAL SOCIETY
OF CHEMISTRY

PAPER

View Article Online
View Journal | View Issue

Check for updates

Cite this: *Nanoscale Adv.*, 2022, **4**, 4847

Nanobubble-based anti-hepatocellular carcinoma therapy combining immune check inhibitors and sonodynamic therapy

Yun Liu,†[acd] ShiQi Yang,†[bc] Qing Zhou,[d] Jun Zhou,[a] Jinlin Li,[e] Yao Ma,[a] Bing Hu,[e] Chaoqi Liu *[bc] and Yun Zhao*[bc]

Hepatocellular carcinoma (HCC) is one of the most common malignancies worldwide, posing a global threat to human healthcare, and current approved treatment strategies do not produce satisfactory outcomes. Here, nanobubbles (NBs) were prepared that carried Immune Check Inhibitors (ICIs), PD-L1 antibody (PD-L1 Ab) and sonodynamic agent CHLORIN E6 (Ce_6); the anti-cancer properties of these NBs were analyzed from the point of view of immune and sonodynamic therapies. The PD-L1 Ab/Ce_6-NBs could inhibit tumor growth through regulating reactive oxygen species (ROS) production, apoptosis, and most importantly, the function of associated immunocytes, including natural killer cells and lymphocytes. The tumor tissues highly expressed markers of immunogenic tumor cell death (ICD) in which the expression of calreticulin (CRT) and ICD-related immune cytokines (CD80, CD86, INF-γ, and IL-2) were increased in PD-L1 Ab/Ce_6-NB treated mice. PD-L1 Ab/Ce_6-NBs also promoted murine spleen lymphocyte proliferation and cytotoxic activity, as well as CD8+ T cell infiltration in the tumor tissues, and downregulation of the PD-L1 protein and mRNA expression. Furthermore, Bax expression was increased and Bcl-2 was inhibited at the mRNA and protein levels in a murine subcutaneous transplanted tumor model. These results indicate that PD-L1 Ab/Ce_6-NBs can induce ROS-dependent ICD to further boost anti-cancer immune responses under the action of targeting the PD-1/PD-L1 immune check point in the tumor microenvironment as a promising therapeutic agent for HCC.

Received 20th May 2022
Accepted 27th September 2022

DOI: 10.1039/d2na00322h

rsc.li/nanoscale-advances

1. Introduction

Hepatocellular carcinoma (HCC) is now the fifth most common cancer in the world and the third highest cause of cancer-related mortality as estimated by the World Health Organization.[1] HCC is associated with a poor five-year survival rate, leading to ∼600 000 deaths each year and causing a global healthcare burden to both developing and developed countries.[2,3] As a common malignant tumor in clinics, HCC is characterized by poor prognosis and ineffective therapeutic options. Recently, immune checkpoint inhibitors (ICIs) undergoing Phase III clinical trials have reshaped the treatment of advanced-stage HCC.[4] Programmed cell death 1 (PD-1) is an inhibitory receptor on the surface of various immune cells. The extracellular domain of PD-1 can be used as an ICI to block the PD-1/programmed death-ligand 1 (PD-L1) signaling pathway, which is one of the mechanisms by which tumor cells escape clearance by the host immune system. PD-1 expressed on the surface of activated T cells can interact with PD-L1, which is expressed in the majority of tumor tissues.[5] Blocking the interaction can activate tumor antigen-specific T cells, and reduce the immune tolerance of T cells, thus enhancing T cell-mediated anti-tumor immunity.[6]

HCC, as a solid tumor, presents a unique microenvironment featuring tortuous vascularity, angiogenesis, hypoxia, and growth-induced solid stresses, among which solid stresses from the abnormal stromal matrix are the main limitations that prevent drugs from penetrating the solid tumor.[7] Therefore, accurate and efficient delivery of theranostic agents into tumor lesions in a controlled manner is critical and remains a significant challenge. However, the absence of vascular supportive tissues in tumors results in the formation of leaky vessels with pores (200 nm to 1.2 μm in diameter) and leads to poor lymphatic drainage, which is the structural basis of the enhanced permeability and retention (EPR) effect.[8] The EPR effect can enhance accumulation and retention of nanobubbles (NBs) at the tumor site.

---

[a] Department of Ultrasound Imaging, The First College of Clinical Medical Science, China Three Gorges University, Yichang, China

[b] Medical College, China Three Gorges University, No.8 Daxue Road, Xiling District, Yichang, China. E-mail: ctgulcq@163.com; ZY_zhaoyun123@163.com

[c] Hubei Key Laboratory of Tumor Microenvironment and Immunotherapy, China Three Gorges University, Yichang, China

[d] Echo Laboratory, Department of Ultrasound Imaging, Renmin Hospital of Wuhan University, Wuhan, China

[e] Department of Ultrasound Imaging, Affiliated Renhe Hospital of China Three Gorges University, Yichang, China

† Contributed equally to this work.

Sonodynamic therapy (SDT) means that after ultrasound irradiation, sonosensitizers can produce cytotoxic substances such as reactive oxygen species (ROS) to achieve the purpose of killing tumor cells; SDT can also induce tumor cell apoptosis and/or necrosis.[9] Furthermore, SDT can produce tumor immunogenicity, thereby mediating an anti-tumor immune response. Both immunotherapy and SDT have unique advantages in the treatment of hepatocellular carcinoma, but they also have disadvantages such as low target efficiency and low drug utilization.

Considering the limitations and challenges in the treatment of liver cancer, rational and multifunctional NBs were designed in the current study. The sonodynamic agent chlorin e6 (Ce_6) and the ICI PD-L1 antibody (PD-L1 Ab) were modified onto the surface of NBs. Using PD-L1 Ab, NBs can deliver Ce_6 in a targeted manner and enhance the concentration and retention of the drug at the tumor site. Ce_6 has higher tumor affinity and reduced toxicity compared with other sonosensitizers. Low-intensity ultrasound irradiation activates Ce_6, which then generates reactive oxygen species (ROS).[10] ROS promotes tumor cell apoptosis and can also trigger immunogenic cell death (ICD), leading to the release of tumor-associated antigens, which subsequently activate immune cells.[11] In terms of immunotherapy, ICD can provoke the expression of tumor antigens and activate T cells by promoting the expression of relevant T cell effectors to enhance the sensitivity and response rate of tumors to ICIs.[12] The modified NBs (PD-L1 Ab/Ce_6-NBs) constructed in the current study were systematically evaluated and not only efficiently inhibited tumor growth, but also synergistically enhanced the immune response, as demonstrated by both *in vitro* and *in vivo* experiments (Fig. 1).

2. Materials and methods

2.1 Preparation of PD-L1 Ab/Ce_6-NBs

PD-L1 Ab/Ce_6-NBs were prepared using the thin-film hydration method.[13] Briefly, DPPC (Avanti, USA), DSPE-PEG2000 (Avanti), DSPE-PEG2000-biotin (Avanti), DC-Chol (Avanti), and Ce_6 (Cayman Chemical, USA) were mixed with chloroform in a mass ratio of 5 : 1:1 : 0.5 : 0.25, respectively, before being transferred to a rotary evaporator to form a homogeneous dark lipid film. Subsequently, PBS and glycerin were mixed in a ratio of 9 : 1, added to the bottle of lipid mixture, and suspended for 1 hour at 45 °C, before being reserved in vials at 4 °C. The air inside the vials was replaced with C_3F_8 (Wuhan Newradar Special Gas Co., Ltd., China), and the vials were oscillated for 60 s before standing at room temperature for 5 min for stratification, in which the lower layer of brown liquid was the biotinylated Ce_6-NBs (biotin-Ce_6-NBs). Finally, biotin-Ce_6-NBs were incubated with biotinylated PD-1 antibody (Ab) for 20 min at room temperature to obtain PD-L1 Ab/Ce_6-NBs. The mass ratios of DPPC, DSPE-PEG2000, DSPE-PEG2000-biotin, DC-chol, and Ce_6 of other types of NBs are shown in Table 1, and other processes were same as the production of PD-L1 Ab/Ce_6-NBs. The

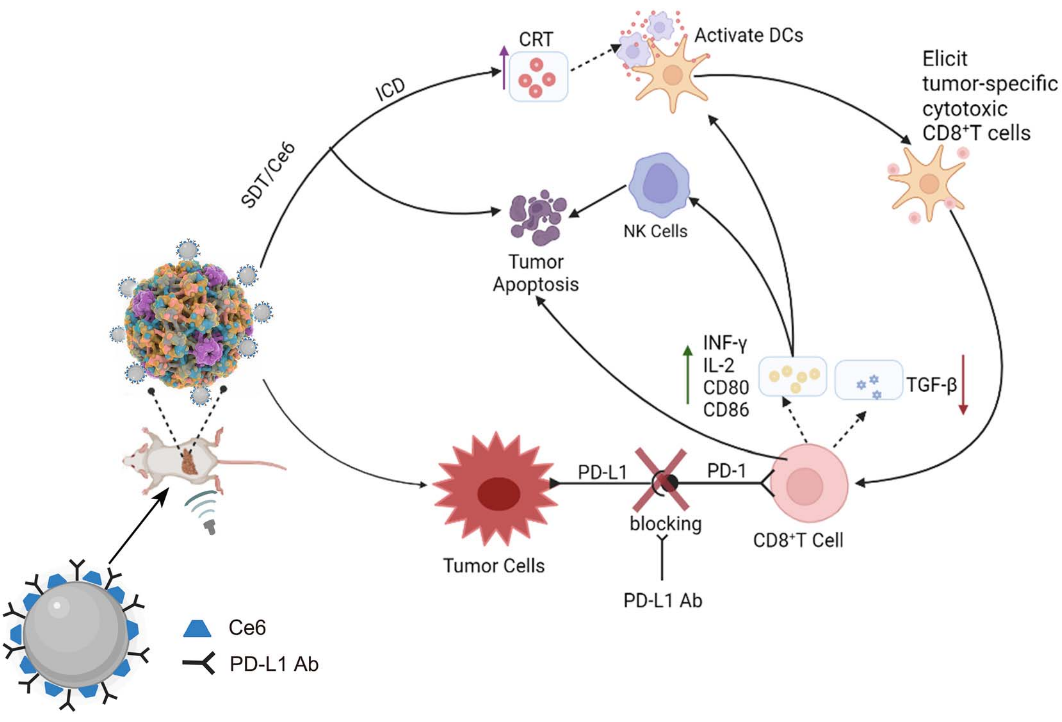

Fig. 1 Schematic illustration of the anti-tumor effect induced by SDT combined with checkpoint blockade for effective cancer immunotherapy. Ce_6 and PD-L1 Ab were loaded into NBs. With ultrasound irradiation, SDT induces ICD at the tumor site, leading to the release of tumor-associated antigens (such as CRT). These antigens activate dendritic cells (DCs) and then elicit proliferation of tumor-specific cytotoxic CD8+ T cells. Meanwhile, SDT markedly improves the sensitivity and response rate of ICIs, thereby synergistically enhancing the effect of PD-L1 Ab in blocking the PD-1/PD-L1 pathway.

Table 1 Mass ratio of ingredients

	DPPC	DSPE-PEG2000	DSPE-PEG2000-biotin	DC-chol	Ce_6
NBs	5	2	0	0.5	0
Ce6-NBs	5	2	0	0.5	0.25
PD-L1 Ab-NBs	5	1	1	0.5	0
PD-L1 Ab/Ce6-NBs	5	1	1	0.5	0.25

prepared NBs were used for the detection of morphology and size. The loading status of Ce_6 in the PD-L1 Ab/Ce_6-NBs was analyzed by using confocal microscopy and full wavelength absorption spectroscopy. The Ce_6 encapsulation efficiency was calculated as previously reported.[14]

2.2 Connection efficiency of biotin-PD-L1 Ab or Ce_6 coating to NBs in PD-L1 Ab/Ce_6-NBs

Briefly, biotin-Ce_6-NBs were incubated with FIFC-streptavidin for 1 h at 37 °C, then biotinylated PD-L1 Ab was added and incubated overnight at 4 °C to prepare FITC-labeled biotinylated PD-L1 Ab/Ce_6-NBs. Flow cytometry was used to detect the connection efficiency of biotin-PD-L1 Ab or/and Ce_6. Confocal microscopy was employed to observe the fluorescence on the surface of PD-L1 Ab/Ce_6-NBs through the red and green channels.

2.3 Cell culture

The murine hepatoma cell line H22 and the human hepatoma cell line HepG2 were purchased from the China Center for Type Culture Collection (CCTCC, Wuhan, China). All cells were maintained in DMEM (Thermo Fisher Scientific, MA, USA) supplemented with 10% heat-inactivated fetal bovine serum (FBS), 100 U mL^{-1} penicillin, and 100 mg mL^{-1} streptomycin and were cultured in a humidified incubator with a 5% CO_2 atmosphere at 37 °C.

2.4 ROS detection

HepG2 cells were seeded in 24-well plates and NBs, Free-Ce_6, Ce_6-NBs, and PD-L1 Ab/Ce_6-NBs, respectively, were added. An ultrasound probe was coated with couplant and tightly attached to the bottom of the 24-well plates (intensity: 1.1 W cm^2; time: 30 s). Next, DCFH-DA (10 mmol L^{-1}) was added to each well and incubated for 30 min. After washing with serum-free DMEM, green fluorescence in the HepG2 cells was observed under a fluorescence microscope (excitation wavelength, 488 nm; emission wavelength, 525 nm)

2.5 Verification of PD-L1 Ab/Ce_6-NBs targeting tumor cells *in vitro*

HepG2 cells were seeded in a 6-well plate (1 × 10^7 per mL), and then PD-L1 Ab/Ce_6-NBs or Ce_6-NBs were added at 37 °C for 30 min. After fixation with 4% paraformaldehyde and incubation with DAPI, the accumulation of the above two types of NBs around HepG2 cells was observed under a fluorescence microscope.

2.6 Contrast-enhanced ultrasound imaging

Four mice with a transplanted tumor, of which the diameter reached 5 ± 2 mm, were selected for further experiments. Mice were narcotized through inhalation of 2% isoflurane (1.2 L min^{-1}) and an electric blanket was utilized to keep them warm during the operation. Contrast-enhanced ultrasound imaging was conducted with a Mindray RESONA7S (Mindray Medical International Co., Ltd. China) equipped with a 14 MHz central frequency linear probe. Mice were injected intravenously *via* the tail vein with 200 μL NBs and PD-L1-Ab/Ce_6-NBs to evaluate the capability of contrast imaging *in vivo*, with quantitative analyses by using Sonamath software (AmbitionT. C., China).

2.7 Fluorescence imaging *in vivo*

The tumor-targeting ability and histological distribution of Ce_6 were evaluated with an IVIS spectrum *in vivo* imaging system for small animals (Xenogen, USA). Free-Ce_6, Ce_6-NBs, and PD-L1 Ab/Ce_6-NBs were intravenously injected into the mice, and the mice were anaesthetized with isoflurane gas at an induction dose of 2–3% and maintenance dose of 1.5–2% prior to imaging. Next, fluorescence FL images were acquired with the IVIS spectrum *in vivo* imaging system (excitation wavelength, 620 nm; emission wavelength, 670 nm) at different time points post-injection (0, 0.5, 1, 3, 6, 9, 12, 24, 36, and 48 h). At 48 h post-injection, the mice were humanely sacrificed and tumors and other organs, including the heart, liver, spleen, lungs, and kidneys, were collected for fluorescence imaging. Frozen sections of tumor tissues were prepared to observe the Ce_6 fluorescence intensity by using a fluorescence microscope (Ti-DH; Nikon Corporation). Semi-quantification was conducted with Image J software 1.51 k (ACEA Bioscience, Inc.; Agilent Technologies, Inc.)

2.8 Animal experiments

H22 hepatoma cells (1 × 10^6 per mL) were injected into the abdomen of male Balb/c mice, and ascites fluid was collected after 6 to 8 days. After centrifugation and washing, H22 hepatoma cells were diluted to 1 × 10^7 per mL and injected subcutaneously into the right anterior armpit of the mice (200 μL per mouse). When the diameter of the transplanted tumor reached 5 ± 2 mm, the mice were involved in the following contrast-enhanced ultrasound experiment.

A total of 42 male Balb/c mice were randomly divided into control, NB, Free-Ce_6, Ce_6-NB, PD-L1 Ab-NB, and PD-L1 Ab/Ce_6-NB groups. Mice except the control group received an injection of the 200 μL corresponding NBs through the tail vein every 2 days for a total of five times, while the control group received

200 μL normal saline. After injection, mice were exposed to ultrasound irradiation with the following parameters: frequency, 1 MHz; intensity, 1.82 W cm^2; time, 120 s; duty cycle, 50%. The longest (L) and shortest (S) diameters of the tumors were measured before injection, and the tumor volume was calculated to obtain the tumor growth curve (tumor volume = 1/2LS^2). The tumor suppression rate was calculated as:

$$\text{Tumor suppression rate}(\%) = \left(1 - \frac{V_1}{m_1} \div \frac{V_2}{m_2}\right) \times 100\%$$

where V_1 is the tumor volume of the experimental group, m_1 is the tumor mass of the experimental group, V_2 is the tumor volume of the control group, and m_2 is the tumor mass of the control group. On the last day, all mice were sacrificed, and the tumors were dissected and collected.

The study was conducted in accordance with the ethical standards and national and international guidelines and was approved by the authors' institutional review board (China Three Gorges University Laboratory Animal Management Committee). BALB/c mice (No. 42010200004317; weight 18–20 g) were purchased from the China Three Gorges University Experimental Animal Center (permission number: SYXK 2017-0061). All animal experiments were carried out in accordance with the guidelines of the National Institutes of Health Guide for the Care and Use of Laboratory Animals and were approved by the China Three Gorges University Laboratory Animal Management Committee (No. 2020B010E). To avoid suffering, animals were sacrificed if clinical conditions were severe.

2.9 Hematoxylin & eosin (H & E)

The size of the excised transplanted tumors was measured, and then for histopathological analysis, the tumors were fixed in 4% paraformaldehyde and embedded in paraffin. The sections were stained with hematoxylin & eosin (H&E) according to standard protocols.

2.10 Histochemistry analysis

An immunohistochemistry assay was applied to evaluate the expression level of proteins as previously described.[15] Briefly, sections of tumor tissues were treated with 3% hydrogen peroxide, blocked with 5% BSA, and incubated overnight at 4 °C with primary antibodies for Bax, Bcl-2, and CRT (Santa Cruz, CA, USA), respectively. Secondary antibodies were introduced and incubated at room temperature for 1 h before being visualized with diaminobenzidine. The stained sections were viewed with an Olympus microscope (Nikon, Tokyo, Japan).

2.11 Immunofluorescence analysis

Tumor sections were fixed with 4% paraformaldehyde for 2 h and permeabilized with 0.1% Triton X-100 for 5 min at 25 °C. The cells were then incubated overnight at 4 °C with CD8 and PD-L1 primary antibody (1 : 200) (Abcam, Cambridge, UK), respectively. Subsequently, a FITC-conjugated anti-mouse IgG antibody was added and incubated at 25 °C for 1 h, and then DAPI was introduced. Images were acquired by confocal laser scanning microscopy (Nikon, Tokyo, Japan).

2.12 Quantitative real-time PCR (qRT-PCR) analysis

The total RNA was isolated from tumor tissues of the different groups of mice using the TRIzol reagent (Thermo Fisher Scientific). cDNA was prepared using a PrimeScript RT Master Mix (Perfect Real Time) (TaKaRa, Beijing, China), according to the manufacturer's instructions. The expression of mRNA was quantified using an Applied Biosystems real-time PCR system with SYBR Premix Ex Taq II (Tli RNaseH Plus) (TaKaRa, Beijing, China). The quantification results were calculated using the $2^{-\Delta\Delta CT}$ method in comparison with GAPDH as the reference mRNA. The primer sequences (5′ to 3′) used for qRT-PCR are listed in Table 2.

2.13 Spleen lymphocyte proliferation assay

The spleens were washed with a Roswell Park Memorial Institute (RPMI) 1640 medium, crushed to isolate the spleen lymphocytes, and passed through a 200-mesh stainless steel sieve to obtain a homogeneous cell suspension. The spleen suspension was washed twice with an RPMI 1640-FBS medium and the recovered spleen lymphocytes were resuspended in TAC lysis buffer for 5 min to remove the erythrocytes. The spleen lymphocytes were then resuspended in RPMI 1640-FBS and seeded in 24-well plates (1 × 10^7 per mL) before being incubated with CFDA-SE (5 μmol L^{-1}). Finally, the spleen lymphocytes were stimulated by tumor antigen (10 μg mL^{-1}) and IL-2 before flow cytometry analysis.

2.14 Cytotoxic T cell (CTL)-specific and natural killer (NK) cell responses

Previously reported methods[14] were adopted for these analyses. Briefly, for CTL-specific activity analysis, cells were stimulated

Table 2 The sequences of primers

Gene	Forward	Reverse
GAPDH	5′-GGTGGTCTCCTGTGACTTCAA-3′	5′-CCACCCTGTTGCTGTAGCC-3′
Bax	5′-TGGTTGCCCTCTTCTACTTTGC-3′	5′-CAGACAAGCAGCCGCTCAC-3′
Bcl-2	5′-CGTCAACAGGGAGATGTCACC-3′	5′-CAGCCAGGAGAAATCAAACAGAG-3′
CD80	5′-TCTCCACGGAAACAGCATCT-3′	5′-CTTACGGAAGCACCCATGAT-3′
CD86	5′-GGCAAGGCAGCAATACCTTA-3′	5′-CTCTTTGTGCTGCTGATTCG-3′
INF-γ	5′-CCATCGGCTGACCTAGAGAA-3′	5′-GATGCAGTGTGTAGCGTTCA-3′
IL-2	5′-GCGAATTCATGATGTGCAAAGTACTG-3′	5′-GCGTCGACTTATTTTTGCAGATATCTCAC-3′
TGF-β	5′-TGACGTCACTGGAGTTGTACGG-3′	5′-GGTTCATGTCATGGATGGTGC-3′
PD-L1	5′-TGCTGCATAATCAGCTACGG-3′	5′-CCACGGAAATTCTCTGGTTG-3′

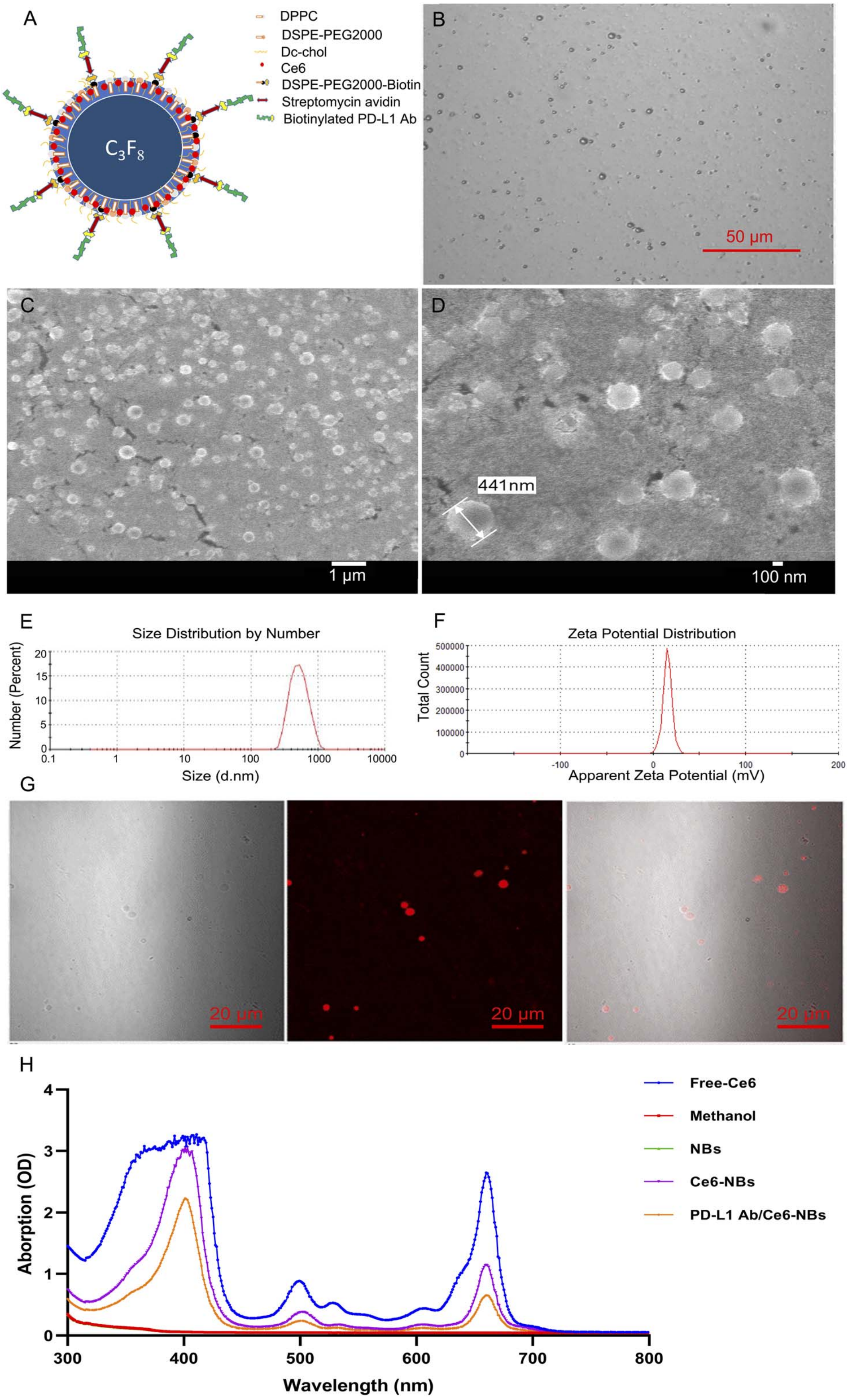

Fig. 2 Characterization of PD-L1/Ce_6-NBs. (A) Structure of PD-L1/Ce_6-NBs. (B) PD-L1 Ab/Ce_6-NBs were observed by confocal microscopy in the white light channel, (×600 magnification), scale bar 50 μm. (C and D) PD-L1 Ab/Ce_6-NBs were observed by scanning electron microscopy at ×10 000 magnification, scale bar 1 μm (C) and ×30 000 magnification, scale bar 100 nm (D). (E) Size distribution of PD-L1 Ab/Ce_6-NBs. (F) Zeta potential of PD-L1 Ab/Ce_6-NBs. (G) Observation of PD-L1 Ab/Ce_6-NBs in a white light channel, red light channel under a confocal microscope (×1000 magnification), scale bar 20 μm. Excitation wavelength 488 nm, emission wavelength 561 nm. (H) Determination of the Ce6 full wavelength absorption spectrum.

by H22 antigen (tumor cell lysis) and IL-2 (50 U per mL) for 48 h. Activated lymphocytes (1×10^7/mL) were then mixed with H22 cells for 3 h in an assay kit. The percentage of lactate dehydrogenase (LDH) cytotoxicity was determined as follows: LDH cytotoxicity (%) = (experimental release − spontaneous release)/(maximum release − spontaneous release) × 100%. For NK cell activity analysis, splenic cells (effector cells) were cultured with H22 cells (target cells) for 3 h at a ratio of 50 : 1. Finally, NK cell activity was measured with a lactate dehydrogenase assay kit (Beyotime Institute of Biotechnology, China).

2.15 TUNEL assay

Apoptosis was detected following the instructions of the TUNEL apoptosis detection kit (Qiyi Biological Technology (Shanghai) Co., Ltd., China), with observation under a fluorescence microscope. Briefly, the sections were incubated with proteinase K reaction solution, while sections of the positive control group were incubated with DNase I buffer. After reacting with TUNEL test solution, the sections were treated with DAPI solution and then observed under a fluorescence microscope.

2.16 Statistical analysis

Statistical analyses were performed using GraphPad Prism 9.0 and SPSS 13.0. The results were compared using one-way analysis of variance (ANOVA) and differences were considered significant at $P < 0.05$. Data are presented as the mean ± standard deviation (mean ± SD).

3. Results

3.1 PD-L1 Ab/Ce_6-NB characterization

To determine the physical and chemical properties of PD-L1 Ab/Ce_6-NBs, the morphology, size, zeta potential, fluorescence, and encapsulation efficiency of the NBs were analyzed. As shown in Fig. 2A, the shell membrane consisted of DPPC, DSPE-PEG2000, DSPE-PEG2000-biotin, Dc-chol, and Ce_6, and the NBs were filled with C_3F_8 and connected to biotin-PD-L1 Ab by the bridge of "avidin–biotin". Under the confocal and scanning electron microscopes (Fig. 2B–D), PD-L1 Ab/Ce_6-NBs were spherical with a smooth surface and were dispersed and uniform. The average particle size and zeta potential of the PD-L1 Ab/Ce_6-NBs were 460 ± 81 nm and 9.9 ± 4.4 mV (Fig. 2E and F). Confocal microscopy observations suggested that the shell membrane of spherical PD-L1 Ab/Ce_6-NBs emitted uniform red fluorescence (Fig. 2G), indicating that Ce_6 with spontaneous red fluorescence had been successfully loaded into the NBs. The absorption spectra of PD-L1 Ab/Ce_6-NBs and Ce_6-NBs after rupture with methanol were consistent with the Free-Ce_6 absorption spectra, while the absorption spectra of NBs and methanol were nearly coincident and showed no obvious absorption peaks. Simultaneously, the maximal absorption peak appeared at a wavelength of 403 nm, and there was no obvious interference of NBs and the methanol absorption peak in this band (Fig. 2H). Comparing the average size, zeta potential, and Ce_6 encapsulation rate, there were no significant differences among the different groups of NBs (Table 3).

3.2 PD-L1 Abs enhance the binding of biotin-Ce_6-NBs to tumor cells *in vitro* and *in vivo*

The positive rate of Ce_6 and biotin-PD-L1 Ab coating to NBs was determined. Flow cytometry analysis suggested that in the single staining group, the Ce_6 coating rate in the Ce_6-NB group was 97.14 ± 2.93%, and the biotin-PD-L1 Ab binding rate in the biotin-NBs was 32.73 ± 4.73%, whereas the Ce_6 and biotin-PD-L1 Ab double-positive staining rate in the PD-L1 Ab/Ce_6-NBs was 63.37 ± 5.53%% (Fig. 3A). This suggests that Ce_6 promotes avidin exposure on the NB surface and enhances avidin binding to the biotin-PD-L1 Ab. PD-L1 Ab/Ce_6-NBs were also observed under a confocal microscope and orange fluorescence could be seen in the merge function, which was the combination of red and green fluorescence, indicating that PD-L1 Ab/Ce_6-NBs were successfully loaded with Ce_6 on the surface and connected to biotin-PD-L1 Ab (Fig. 3B). By immunofluorescence staining, the surface of H22 cells emitted green fluorescence from staining with the FITC-PD-L1 antibody, suggesting that the PD-L1 antigen was expressed on the surface of H22 cells (Fig. 3C), and this was also supported by flow cytometry analysis (Fig. 3D). To demonstrate the targeting capability of PD-L1 Ab/Ce_6-NBs, HepG2 cells were incubated with PD-L1 Ab/Ce_6-NBs or Ce_6-NBs before being fixed and examined by using immunofluorescence staining and a fluorescence microscope. Ce_6-NBs with red fluorescence were sparsely distributed around HepG2 cells, whereas PD-L1 Ab/Ce_6-NBs with spot-like red fluorescence were densely distributed on the surface of HepG2 cells (Fig. 3E), indicating the active targeting ability of PD-L1 Ab/Ce_6-NBs. The modified NBs were effective as an ultrasound contrast agent in tumors (Fig. 3F), with a higher area under the curve (AUC) and maximum intensity (I_{max}) seen in the PD-L1 Ab/Ce_6-NB group

Table 3 Determination of the average size, zeta potential and Ce_6 encapsulation rate[a]

	Average size (nm)	Zeta potential (mV)	Ce6 encapsulation rate (%)
NBs	456 ± 102	10.3 ± 3.6	
Ce6-NBs	427 ± 97	11.2 ± 4.1	73.37 ± 6.09
PD-L1 Ab-NBs	537 ± 119	9.7 ± 3.8	
PD-L1 Ab/Ce6-NBs	460 ± 81	9.9 ± 4.4	71.22 ± 4.26

[a] (Data are presented as the mean ± SEM. $P > 0.05$, *vs.* control).

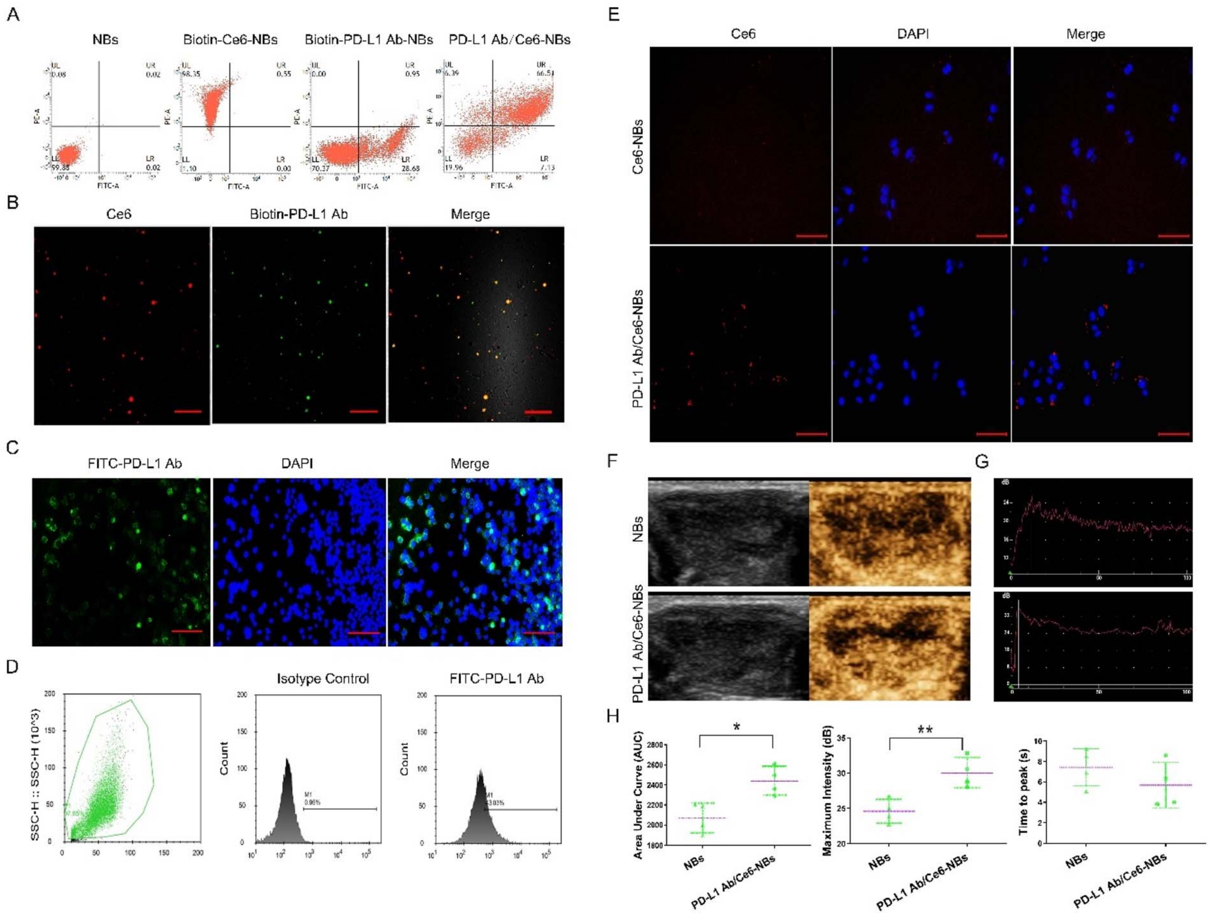

Fig. 3 Targeting verification of PD-L1Ab/Ce6-NBs. (A) Single staining binding rate of Ce_6 or biotin-PD-L1 Ab in NBs, biotin-Ce_6-NBs, and biotin-PD-L1 Ab-NBs, and double-staining positive rate of Ce_6 and biotin-PD-L1 Ab in PD-L1 Ab/Ce_6-NBs obtained by flow cytometry. (B) Observation of PD-L1 Ab/Ce_6-NBs by confocal microscopy (×200 magnification), scale bar 100 μm. (C) PD-L1 antigen expression on the H22 cell surface by fluorescence microscopy (×200 magnification), scale bar 100 μm. (D) Flow cytometry analysis of PD-L1 protein expression in H22 cells. (E) Targeting of PD-L1 Ab/Ce_6-NBs *in vitro* (×200 magnification), scale bar 100 μm. (F) Contrast-enhanced ultrasound in a subcutaneous transplanted tumor murine model of hepatocellular carcinoma *in vivo*. (G) Real-time contrast ultrasound curve of NBs and PD-L1 Ab/Ce_6-NBs. (H) Analysis of quantitative parameters AUC, I_{max}, and TTP of contrast-enhanced ultrasound among NB and PD-L1 Ab/Ce_6-NB groups. Data are presented as the mean ± SEM. *$P < 0.05$, **$P < 0.01$ *vs.* NBs.

compared with the NB group, while the time to peak (TTP) had no significance. After evaluating the imaging effect of the two groups of NBs in the tumor area and the contrast parameters, the contrast agent in both groups manifested a good effect of enhanced imaging in the tumor tissue, and the AUC and I_{max} of the PD-L1 Ab/Ce_6-NB group were significantly higher compared with those of the NB group (Fig. 3G and H). This suggested that both the NBs and the PD-L1 Ab/Ce_6-NBs can perform the function of *in vivo* ultrasound imaging, among which the cumulative concentration and maximum peak intensity of PD-L1 Ab/Ce_6-NBs during the same period of time in the tumor tissue were markedly higher.

3.3 PD-L1 Ab enhances the accumulation and retention of biotin-Ce_6-NBs at tumor sites *in vivo*

The distribution and intensity of Ce_6 red fluorescence inside the body of different groups of mice before and after injection were studied. The obtained images suggested that with increasing time, the fluorescence declined in organs but strengthened in tumors, especially 6 h after injection when the fluorescence reached its peak. The concentration of Ce_6 in the tumor of the PD-L1 Ab/Ce_6-NB group was significantly higher compared with that of the Free-Ce_6 group from 3 h after tail vein injection. Furthermore, Free-Ce_6 and Ce_6-NBs disappeared at the tumor site after 36 h, while the red fluorescence signal of the PD-L1 Ab/Ce_6-NB group was sustained up to 48 h (Fig. 4A–D). These results suggest that PD-L1 Ab/Ce_6-NBs can significantly enhance the local enrichment of Ce_6 in tumor tissues and prolong the metabolic time of Ce_6 in tumor tissues. Fluorescence imaging suggested that the red fluorescence was strongest in the tumor compared with the liver and kidneys. Furthermore, in terms of the tumor, the fluorescence signal in PD-L1 Ab/Ce_6-NB mice was much stronger compared with that in Free-Ce_6 mice. A limited amount of light red fluorescence was seen in the tumor site of the mice in the Free-Ce_6 group, while the tumor tissues in the Ce_6-NB group and the PD-L1 Ab/Ce_6-NB group exhibited sheet-like collective red fluorescence (Fig. 4E). Moreover, the red

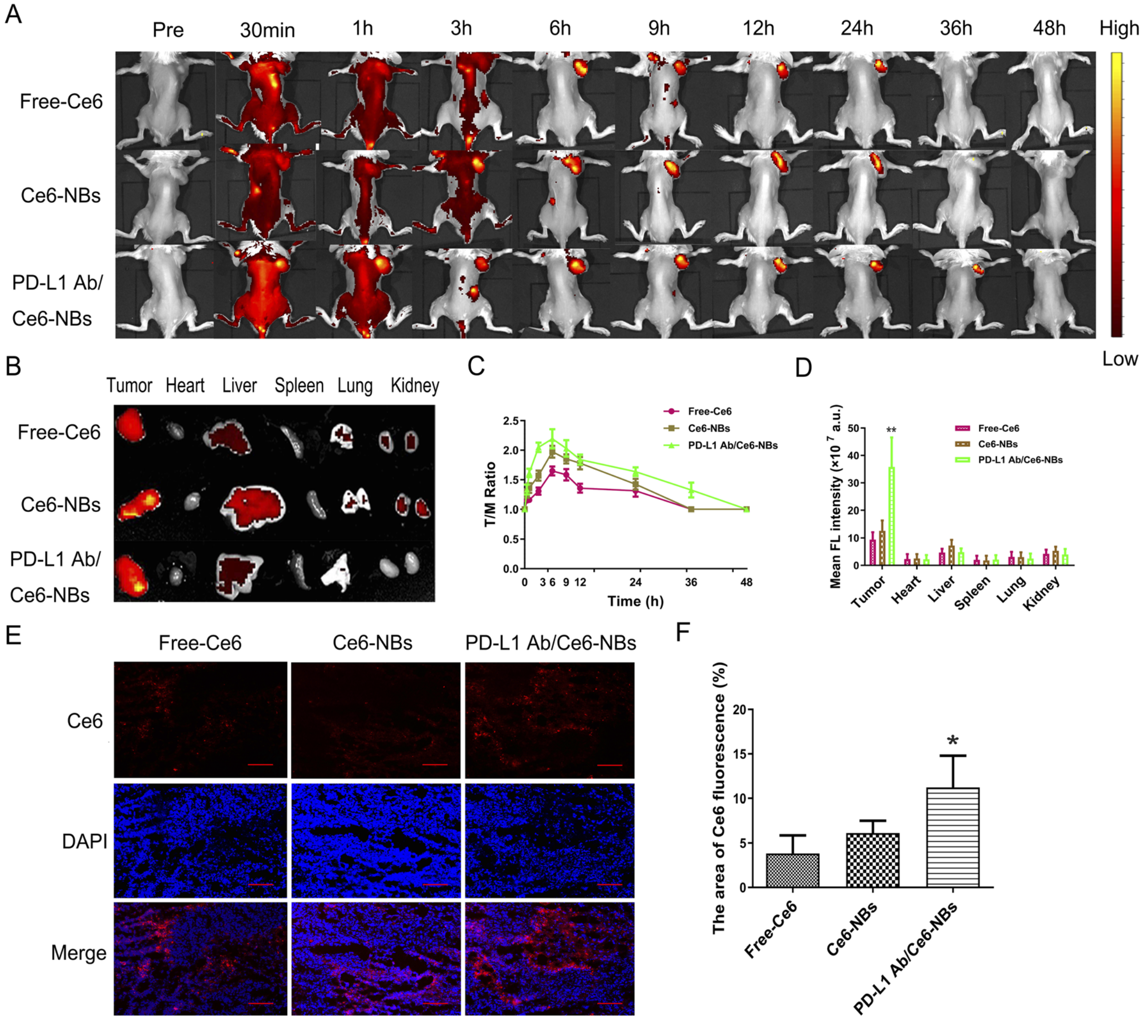

Fig. 4 Detection of Ce_6 in a subcutaneous transplanted tumor murine model of hepatocellular carcinoma. (A) Distribution and intensity of red fluorescence in Free-Ce_6, Ce_6-NB, and PD-L1 Ab/Ce_6-NB mice before and after injection. (B) Fluorescence signal of Ce_6 in the tumor and other organs of different groups of mice after 48 h. (C) Fluorescence quantitative analysis of tumor tissues of three groups of mice within 48 h. (D) Fluorescence quantitative analysis in the tumor and other organs of different groups of mice after 48 h. (E) Fluorescence aggregation of Ce_6 in the tumor area was observed for different groups of mice. (F) Quantitative analysis of Ce_6 red fluorescence in tumor tissue. Data are presented as the mean ± SEM. $^*P < 0.05$, $^{**}P < 0.01$ *vs.* Free-Ce_6.

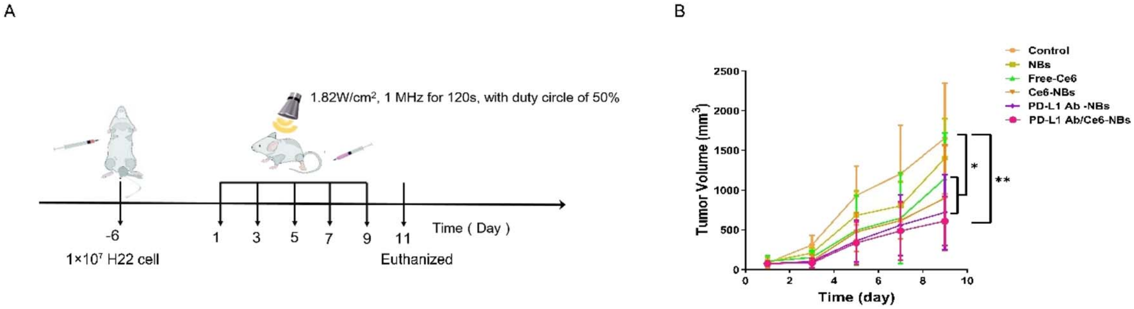

Fig. 5 Inhibitory effect of PD-L1 Ab/Ce_6-NBs on the subcutaneous transplanted tumor of hepatocellular carcinoma in mice. (A) Schematic illustration of the therapeutic formulations. The interval treatment mode is adopted every other day for a total of five treatments; ultrasound parameters are as follows: frequency, 1 MHz; intensity, 1.82 W cm^2; time, 120 s; duty cycle, 50%. (B) Tumor volume growth curve, $^*P < 0.05$, $^{**}P < 0.01$ *vs.* control.

fluorescence of the PD-L1 Ab/Ce_6-NB group was significantly stronger compared with that of the Free-Ce_6 group, which also suggested that PD-L1 Ab/Ce_6-NBs can significantly improve the enrichment ability of Ce_6 at the tumor site (Fig. 4F).

3.4 The effects of PD-L1 Ab/Ce_6-NBs on tumor progression in a murine transplanted tumor model

Tumor growth of the control group increased exponentially, while the tumor growth rates of the other treatment groups were slower compared with that of the control group, with the tumor growth curve of the PD-L1 Ab/Ce_6-NB mice exhibiting the slowest growth (Fig. 5). The tumor volume inhibition rates of Ce_6-NB, PD-L1 Ab-NB, and PD-L1 Ab/Ce_6-NB groups were 45.46%, 56.47% and 63.14%, respectively, while, the mass inhibition rates were 36.49%, 53.15% and 67.80%, respectively. Among them, the PD-L1 Ab/Ce_6-NB group manifested the best tumor suppression effect, and the tumor suppression rate was significantly higher compared with those of the control group (Table 4).

3.5 SDT augments the anti-tumor effect through induction of ICD

The generation of ROS was observed under a confocal microscope and only a limited amount of dim green fluorescence was seen in the NB group. The HepG2 cells from the Free-Ce_6, Ce_6-NB, and PD-L1 Ab/Ce_6-NB groups all showed strong green fluorescence, with the Ce_6-NB and PD-L1 Ab/Ce_6-NB groups showing the brightest green fluorescence and no marked difference between these two groups (Fig. 6A). This indicates that the Ce_6 coating on the NBs does not reduce the ROS effect of Ce_6 but does, in turn, promote the accumulation of Ce_6 in HepG2 cells and enhance the ROS effect.

Calreticulin (CRT) is a common and highly conserved endoplasmic reticulum calcium-binding protein that is a decisive multifunctional protein for the recognition and phagocytosis of apoptotic cells. SDT is induced by ROS, cavitation, and thermal effects. Concurrent to tumor cell necrosis or apoptosis, SDT will promote the exposure of calreticulin, as an immune activation molecule, stimulate the immunogenicity of tumor tissues, and facilitate DCs to improve recognition of tumor tissues, thereby enhancing the immune killing activity of tumors. Histochemistry analysis suggested that the expression of CRT in each treatment group of mice showed an upregulation trend, which may be related to ultrasound-mediated NB bursting, among which the Ce_6 treatment groups (Free-Ce_6, Ce_6-NBs, and PD-L1 Ab/Ce_6-NBs) showed the most significant increase in CRT expression (Fig. 6B and D). This indicates that Ce_6 can enhance the immunogenicity of tumor tissues by promoting the expression of CRT, thus laying the foundation for synergistically enhancing immunotherapy.

NK cells are indispensable immune cells that play a crucial role in immune surveillance and are activated through ICD induction. Compared with the control group, NK cell killing was markedly enhanced in the Free-Ce_6, Ce_6-NB, PD-L1 Ab-NB, and PD-L1 Ab/Ce_6-NB groups, and a significant difference was observed in the Ce_6-NB, PD-L1 Ab-NB, and PD-L1 Ab/Ce_6-NB groups (Fig. 6C, E and F).

Tumor-related immune cytokines that are released by activated macrophages, CTL, and NK cells, also hold the key to tumor immunotherapy.[16] INF-γ shows immunoregulatory effects such as activating macrophages, promoting the maturation of CTL, and enhancing the killing activity of NK cells. CD80 and CD86 are markers related to the maturation of DCs, and CD80 is a costimulatory factor when CD86 activates T lymphocytes. IL-2 can induce a series of cytokine cascades, maintain the proliferation of CD4+ and CD8+ cells, and plays a key role in immune regulation, while TGF-β is activated by regulatory T cells (Tregs). The crucial factor is immunosuppression, which can inhibit the activation of helper T cells and killer T cells by inducing Tregs, thereby suppressing the immune response. Therefore, changes in the expression of INF-γ, CD80, CD86, IL-2, and TGF-β have an important impact on the tumor immune microenvironment. As shown in Fig. 7, in the PD-L1 Ab-NB and PD-L1 Ab/Ce_6-NB groups, the expression of INF-γ, CD80, CD86, and IL-2 was significantly upregulated, while the expression of TGF-β was significantly downregulated, compared with the control group.

3.6 PD-L1 Ab/Ce_6-NBs augment the anti-tumor effect through enhancing tumor antigen-specific T cell induction

PD-L1 Ab blocked the PD-1/PD-L1 pathway and killed PD-L1 positive tumor cells. Consequently, the expression of the PD-L1 protein and mRNA was found to be significantly downregulated in the PD-L1 Ab-NB and PD-L1 Ab/Ce_6-NB groups, among which the latter group showed the most marked difference (Fig. 8). This indicated that NBs can smoothly transport PD-L1 Ab to the tumor and bind to PD-L1 on the

Table 4 Tumor volume and mass tumor inhibition rate

Group	Size (mm^3)	Volume inhibition rate (%)	Weight (g)	Weight inhibition rate (%)
Control	1653.44 ± 697.61	0	2.22 ± 0.85	0
NBs	1404.73 ± 491.44	15.04	2.15 ± 0.61	3.27
Free-Ce6	1148.19 ± 568.74	30.56[a]	1.76 ± 0.50	20.60
Ce6-NBs	901.77 ± 664.19	45.46[a]	1.41 ± 0.64	36.49[a]
PD-L1 Ab-NBs	719.78 ± 475.64[a]	56.47[a]	1.04 ± 0.55	53.15[a]
PD-L1 Ab/Ce6-NBs	609.49 ± 306.90[a]	63.14[a]	0.7125 ± 0.37[a]	67.80[a]

[a] (Data are presented as the mean ± SEM. *$P < 0.05$ *vs.* control; **$P < 0.01$ *vs.* control).

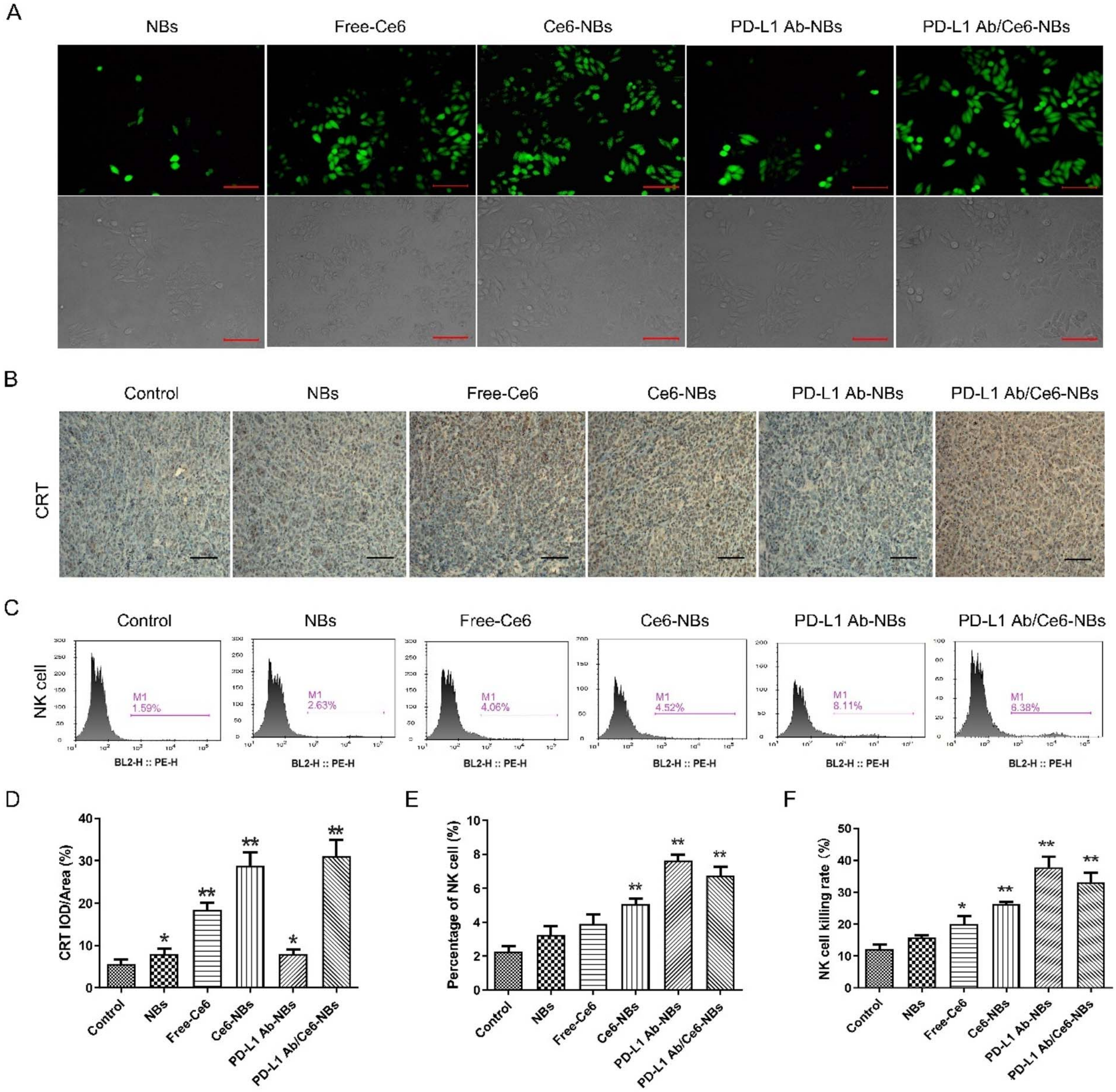

Fig. 6 Detection of ROS and apoptosis in tumor tissues. (A) Production of ROS in tumor cells of different groups under fluorescence microscopy (×200 magnification), scale bar 100 μm. (B) Histochemistry analysis of CRT in tumor tissues, (×200 magnification), scale bar 100 μm. (C) Expression percentage of NK cells in the spleen. (D) Protein expression of CRT. (E and F) Analysis of the percentage of NK cells and NK killing ability. $^{*}P < 0.05$, $^{**}P < 0.01$ *vs.* control.

surface of tumor cells, thereby playing the role of an immune checkpoint blocker and effectively blocking the PD-1/PD-L1 signal pathway and altering the expression of immune cells and immune factors in tumor tissues to fulfill the purpose of immunotherapy.

Lymphocyte proliferation can directly reflect the condition of immunity. Flow cytometry analysis revealed that there was active proliferation of splenic lymphocytes in the PD-L1 Ab-NB and PD-L1 Ab/Ce_6-NB groups (Fig. 9A), especially in the former group, which had a proliferation index that was 3.8 times that of the control group (Fig. 9D). This indicated that PD-L1 Ab can significantly increase the proliferation ability of splenic lymphocytes and stimulate immunity in the body. Furthermore, the percentage of CD8+ expression in the PD-L1 Ab-NB and PD-L1 Ab/Ce_6-NB groups was approximately twice that of the control group (Fig. 9B and E), indicating that NBs with PD-L1 Ab can better promote the proliferation and transformation of T cells and boost the number of CTLs to exert anti-tumor effects. CD8+ T cells are instrumental in tumor immunotherapy and can be activated and differentiated into CTLs through the stimulation of tumor antigens before infiltrating into the tumor microenvironment, and they can specifically recognize tumor antigen peptides, thereby achieving the purpose of killing tumor cells. Fluorescence analysis suggested that compared with control and NB groups, green fluorescence was strengthened in the Free-Ce_6, Ce_6-NB, PD-L1 Ab-NB and PD-L1 Ab/Ce_6-

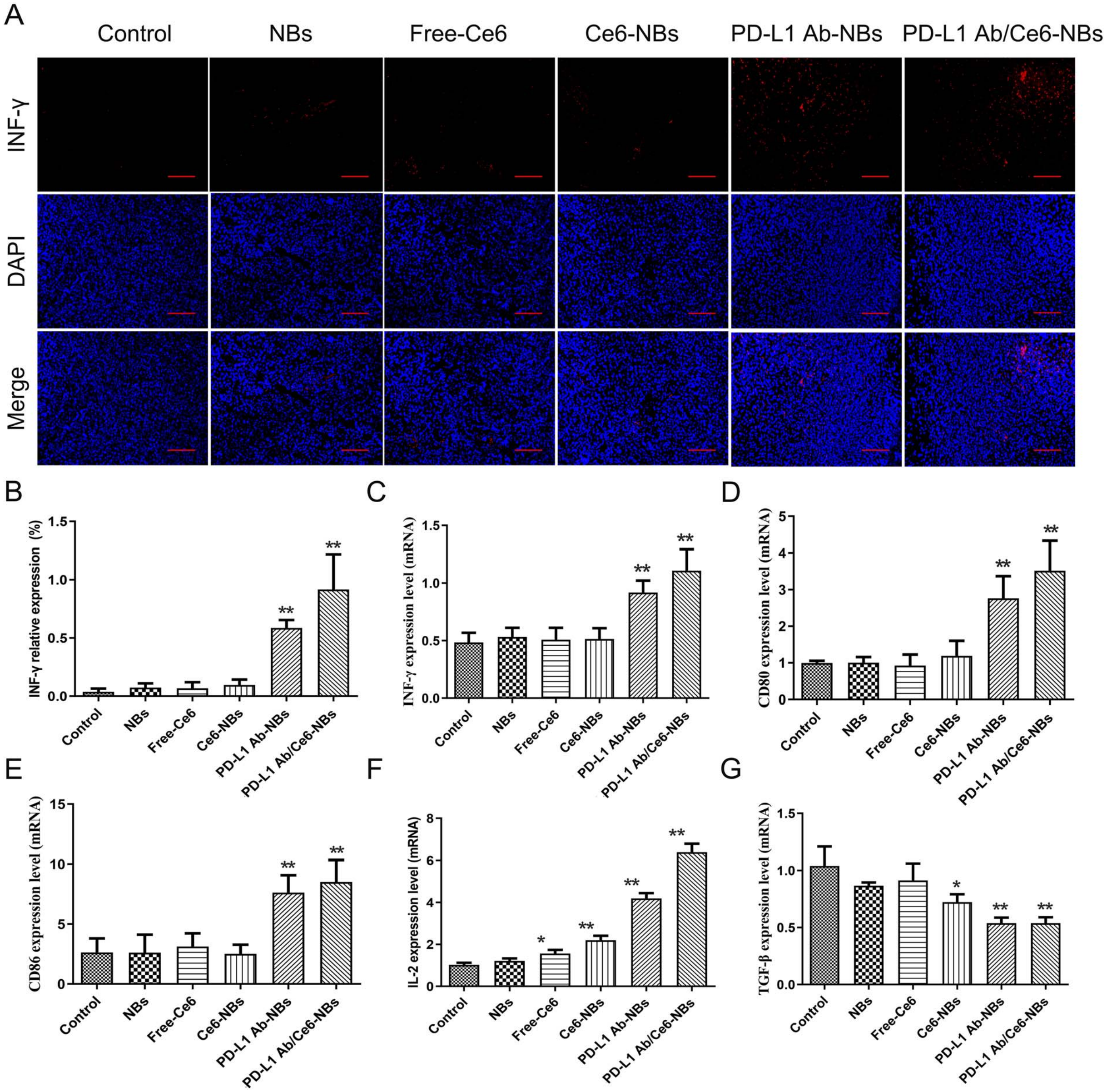

Fig. 7 Detection of immune-associated factors. (A) Immunofluorescence analysis of INF-γ in tumor tissues (×200 magnification), scale bar 100 μm. (B and C) INF-γ protein and mRNA expression in tumor tissues. (D–G) CD80, CD86, IL-2 and TGF-β mRNA expression in tumor tissues. $^{*}P < 0.05$, $^{**}P < 0.01$ *vs.* control.

NB groups, with the strongest green fluorescence detected in the PD-L1 Ab/Ce$_6$-NB group (Fig. 9C). Quantitative analysis of the fluorescence revealed that, compared with the control group, the expression of CD8+ T lymphocytes was significantly increased and the highest expression was observed in the PD-L1 Ab-NB and PD-L1 Ab/Ce$_6$-NB groups (Fig. 9F). Using H22 cells as target cells and CTLs stimulated by tumor antigens as effector cells, CTL killing was enhanced in the Free-Ce$_6$, Ce$_6$-NB, PD-L1 Ab-NB, and PD-L1 Ab/Ce$_6$-NB groups compared with in the control group, and the killing ratio was most significant in the PD-L1 Ab/Ce$_6$-NB group (Fig. 9G).

3.7 PD-L1 Ab/Ce$_6$-NBs augment the anti-tumor effect through promoting apoptosis

Both Ce$_6$ and PD-L1 Ab along with NBs induced tumor cell apoptosis. Therefore, the pathological conditions of tumor tissues were examined by HE staining. In the control group, the tumor cells were arranged in a disorderly manner, with no obvious area of necrosis, and there was obvious heterogeneity, large and dark nuclei, and a high nucleoplasmic ratio. In the other treatment groups, the number of tumor cells was reduced, with nuclear pyknosis and dissolution, and homogenous degeneration and necrotic areas; the PD-L1 Ab/Ce$_6$-NB group manifested the most obvious pathological features (Fig. 10A).

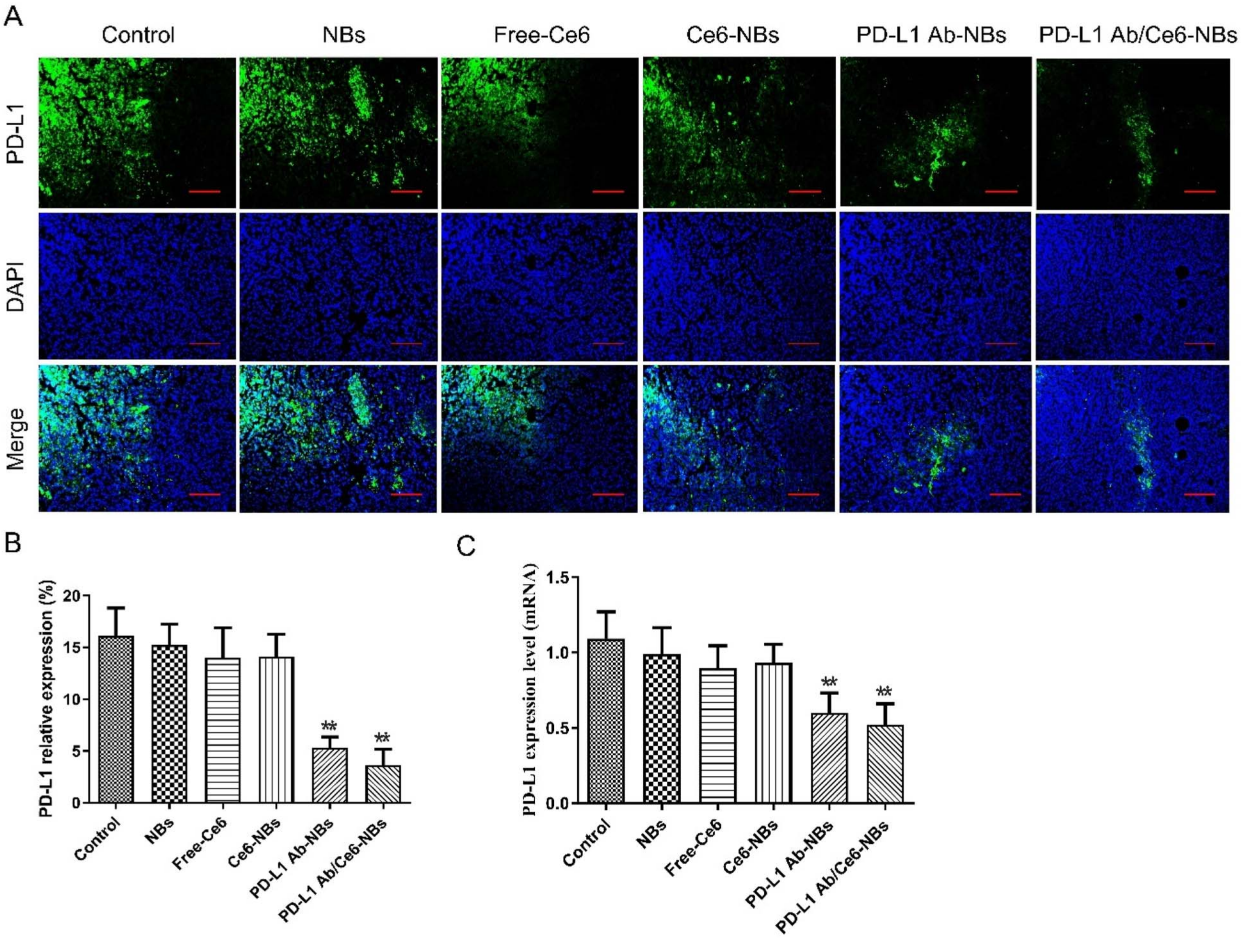

Fig. 8 Detection of PD-L1 in tumors. (A) Immunofluorescence analysis of PD-L1 in tumors (×200 magnification), scale bar 100 μm. (B) Relative expression of PD-L1 in tumors. (C) mRNA expression of PD-L1 in tumors. $^{**}P < 0.01$ *vs.* control.

To further quantify the degree of apoptosis in the tumors, the formation of apoptotic cells was analyzed by TUNEL assay. Green fluorescence for TUNEL staining was observed in each group, among which the Ce_6-NBs and PD-L1 Ab/Ce_6-NBs manifested the brightest green fluorescence, and the highest apoptosis rate was observed in the PD-L1 Ab/Ce_6-NB group (Fig. 10B and C).

To further study the mechanism of the pro-apoptotic effect of NBs on tumor cells, the protein and mRNA expression levels of Bax and Bcl-2 were examined in the different experimental groups. Compared with the control group, the expression of the Bax protein and mRNA in each treatment group was upregulated, while the expression of the Bcl-2 protein and mRNA was downregulated, with the most significant difference observed in the PD-L1 Ab/Ce_6-NB group (Fig. 11).

4. Discussion

In this study, we designed and prepared lipid nanobubbles carrying Ce_6 and PD-L1 Ab (PD-L1 Ab/Ce_6-NBs), and the average particle size and zeta potential of the PD-L1 Ab/Ce_6-NBs were 460 ± 81 nm and 9.9 ± 4.4 mV, respectively. PD-L1 Ab/Ce_6-NBs had uniform particle sizes, good dispersion, high Ce_6 entrapment efficiency, and met the requirements of a molecular-targeted ultrasound contrast agent. As a solid tumor, HCC provides a unique tumor microenvironment, with features such as a lack of vascular tissue support, the frequent formation of porous channels between tumor vascular endothelial cells, and a vascular endothelial space of approximately 1 μm.[17] Therefore, the NBs with a particle size of approximately 500 nm prepared in the current study are theoretically sufficient to pass through the vascular endothelial space of HCC by EPR.[18]

The change of immune microenvironment are involved in almost the whole process of HCC, and ICI-based strategies are a potential major approach in anti-cancer treatment for advanced-stage HCC.[19] However, it is difficult for ICIs to accumulate in solid tumors, which results in low antibody bioavailability and a poor curative effect. To tackle this problem, some scholars have tried to combine ICIs with nanoparticle delivery systems to enhance the accumulation of medications in diseased tissues and reduce adverse reactions including off-target effects.[20,21] Ishijima *et al.*[22] prepared an EREG monoclonal antibody-phase change nano-microbubble complex (9E5-NBs) that could target tumor cells, and *in vitro* experiments proved that the delivery rate of 9E5-NBs to tumor sites was as high as 97.8%, and when combined with ultrasound irradiation,

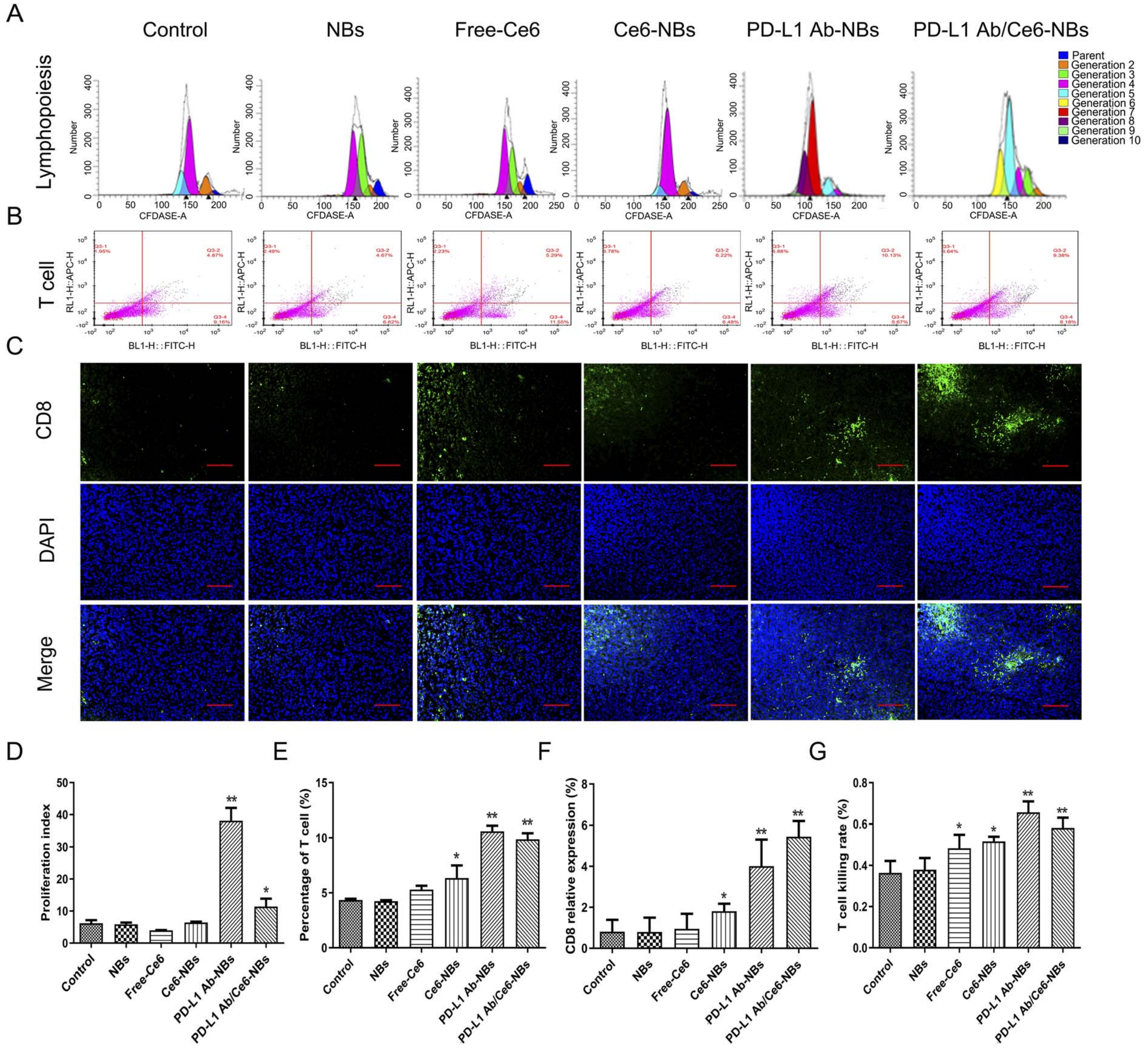

Fig. 9 Detection of splenic lymphocytes and CD8+ T cells. (A and B) Flow cytometry analysis of the spleen lymphocyte proliferation index and percentage of CD8+ T lymphocytes. (C) Immunofluorescence detection of CD8+ T lymphocytes in tumor tissues (×200 magnification), scale bar 100 μm. (D) Spleen lymphocyte proliferation index. (E) Percentage of CD8+ T cells in the spleen. (F) Relative expression of CD8+ T cells in tumor tissues. (G) CTL killing ratio. $^*P < 0.05$, $^{**}P < 0.01$ *vs.* control.

approximately 57% of tumor cells were killed. Inspired by this result, we attempted to connect the biotinylated PD-L1 Ab ligand to the surface of the biotinylated NB shell membrane through the "avidin-biotin" bridge to achieve a combination of ICIs and SDT in the current study. Ce_6 and biotin-PD-L1 Ab had a high connection rate to NBs in PD-L1 Ab/Ce_6-NBs. In addition, PD-L1 Ab could enhance Ce_6 accumulation and retention at tumor sites.

Targeted therapy for cancer can be significantly enhanced by selective tissue localization, but the predominant limited therapeutic effect of this approach is antigen expression on hepatoma cells.[23,24] Therefore, the PD-L1 protein expression level in HCC cells was analyzed and found to be 40.56 ± 3.82%, and PD-L1 Ab/Ce_6-NBs showed an effective targeting ability to HCC cells *in vitro* and *in vivo*. The immunotherapy strategy can also be limited by changes in the tumor immune microenvironment. Some associated cytokines can significantly inhibit the immunogenicity of tumor cells and affect the therapeutic efficacy of ICIs. For example, indoleamine 2, 3-dioxygenase (IDO), interleukin-10 (IL-10), and TGF-β can inhibit the maturation of DCs, leading to the attenuation of tumor-associated antigens (TAAs).[25] Meanwhile, tumor cells can also reduce the immune response by downregulating the expression of major histocompatibility complex I (MHC-I).[26,27] Therefore, improving the specific response rate of the body to ICIs and strengthening the immunogenic exposure of tumor cells are key to improving the efficacy of immunotherapy.

Ce_6 is a sonosensitizer that has specific accumulation and retention at the tumor site and can be excited by ultrasound to maximize sono-sensitivity,[28] a process called SDT. Data from the

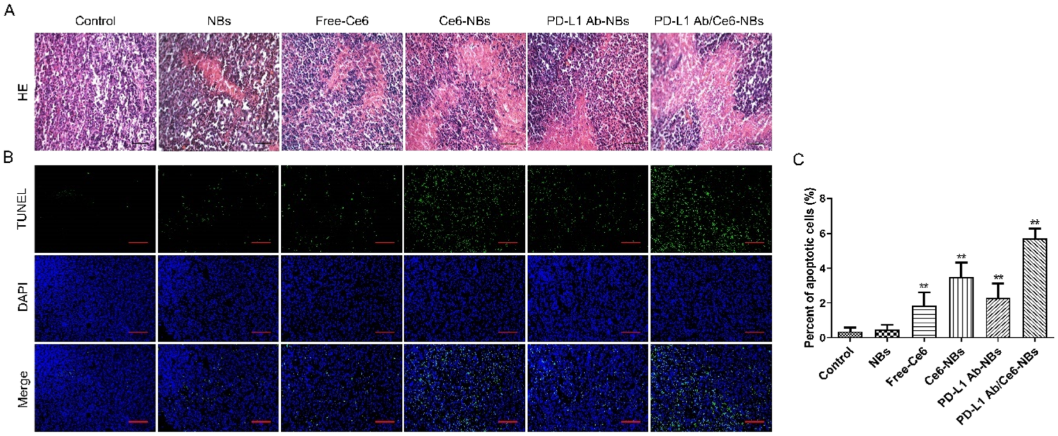

Fig. 10 Necrosis of tumor tissues. (A) HE-stained sections. (B and C) TUNEL detection of tumor tissues (×200 magnification), scale bar 100 μm. $^{**}P < 0.01$ *vs.* control.

current study indicated that PD-L1 Ab/Ce$_6$-NBs can significantly upregulate the expression of Bax, a pro-apoptotic protein, and downregulate the expression of Bcl-2, an anti-apoptotic protein, thereby promoting apoptosis, which is closely related to the release of ROS by SDT. Furthermore, SDT can trigger immune responses by ICD.[29] During the process of ICD, CRT everts and is exposed, and as an immune activation molecule, CRT can promote the activation and maturation of DCs and phagocytose tumor cells to produce immune killing activity against tumors with the same markers.[30] Consequently, CRT is an indispensable factor in SDT to initiate an anti-tumor immune response. To verify how PD-L1 Ab and Ce$_6$ in the PD-L1 Ab/Ce$_6$-NBs elicit a synergistic anti-tumor effect, the expression of CRT in tumor tissues was examined. The Ce$_6$-NBs markedly increased the expression of the CRT protein, compared with the control groups, suggesting that Ce$_6$-mediated SDT can cause CRT eversion, leading to immunogenic death and stimulating an immune response. These results were consistent with the report of Hodge *et al.*,[31] and this is a reasonable explanation of why the PD-L1 Ab/Ce$_6$-NBs showed enhanced mediation in the

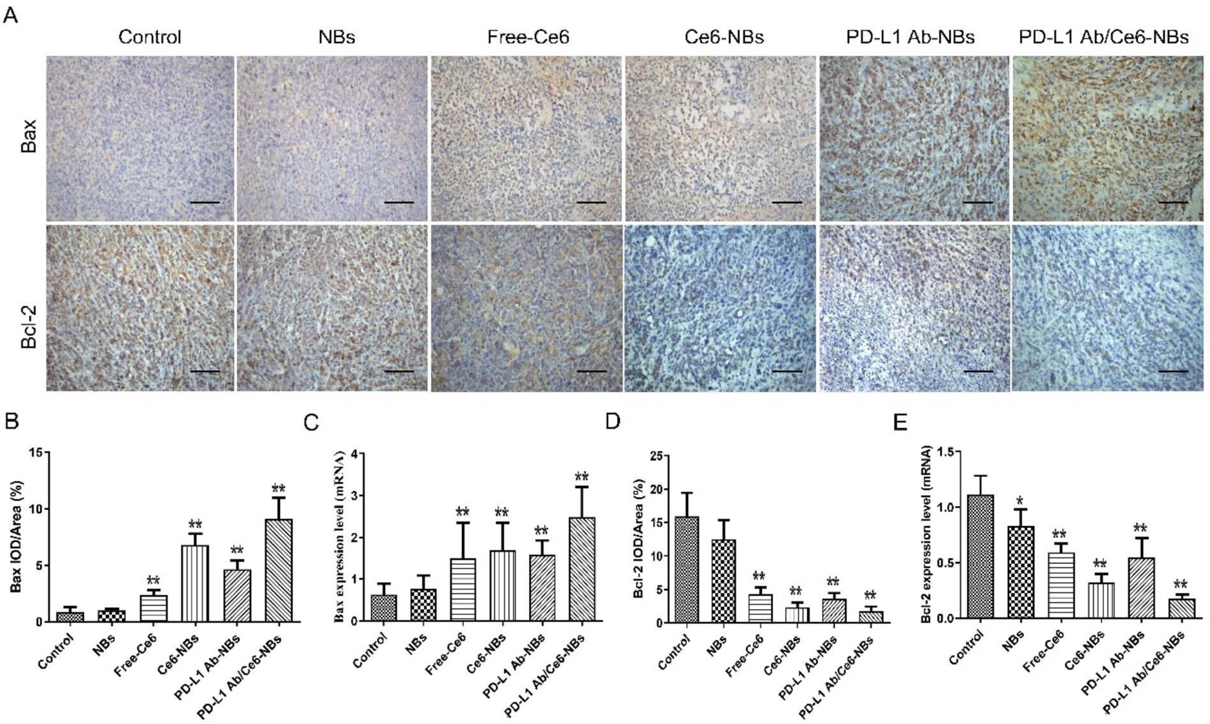

Fig. 11 Apoptosis-associated protein and gene detection. (A) Histochemistry detection of Bax and Bcl-2 proteins in tumor tissues (×200 magnification), scale bar 100 μm. (B and C) Protein and mRNA expression of Bax. (D and E) Protein and mRNA expression of Bcl-2. $^{*}P < 0.05$, $^{**}P < 0.01$ *vs.* control.

immune microenvironment in tumor tissues compared with the PD-L1-NB group. SDT can induce the immunogenic death of tumor cells, thereby enhancing the response rate of ICIs.[32] The PD-L1 Ab/Ce_6-NBs exhibited a good anti-HCC therapeutic effect *in vivo*, with tumor volume and mass inhibition rates of 63.14% and 67.80%, respectively.

PD-L1 Ab/Ce_6-NBs predominantly exert their anti-HCC effects through the following processes: (1) targeting mechanism. First, NBs can pass through the gap of the tumor vascular endothelial cells due to the EPR effect to achieve the purpose of passively targeting tumor tissue; EPR is the main driving force of NB aggregation in the tumor. Secondly, PD-L1 is highly expressed on the surface membrane of hepatoma cells, and NBs carrying PD-L1 Ab showed an enhanced targeting ability to hepatoma cells compared with control NBs, thereby promoting the accumulation of medications at the tumor site. (2) Ultrasound-targeted microbubble destruction (UTMD): UTMD can cause the oscillation and rupture of NBs by local ultrasound, resulting in a series of biological effects such as cavitation, sonoporation, and acoustic radiation force, which can worsen the damage of tumor capillaries, enhance the permeability of the vascular endothelial cell membrane, and promote the accumulation of Ce_6 and PD-L1 Ab at tumor tissues. (3) Ameliorated immune tolerance in the tumor microenvironment: after PD-L1 Ab/Ce_6-NBs accumulate at the tumor site, PD-L1 Ab can function as an ICI, specifically blocking the PD-1/PD-L1 pathway. In addition, PD-L1 Ab can activate CD8+ T cells and induce their differentiation into CTLs, promoting the secretion of immunoregulatory factors CD80, CD86, IL-2, and INF-γ in tumor tissues, while inhibiting the production of immunosuppressive factor TGF-β. (4) Tumor cell apoptosis induced by PD-L1 Ab/Ce_6-NBs: this study demonstrated that PD-L1 Ab/Ce_6-NBs can accumulate in tumor tissues more effectively and for a longer period of time, and can generate a large amount of ROS under ultrasound irradiation, which in turn induced tumor cell apoptosis and necrosis. Moreover, PD-L1 Ab/Ce_6-NBs can exaggerate the killing ability against tumor cells by boosting the proliferation and function of NK cells and CD8+ T cells. (5) Immune regulation and synergistic anti-tumor activity with SDT: internal CRT is exposed on the surface of tumor cells by SDT, which activates DCs and increases the infiltration of CD8+ T cells at the tumor site. In addition, SDT can cause tumor immunogenic death, which facilitates T cell recognition, thereby markedly improving the sensitivity and response rate of ICIs. Lin *et al.*[33] prepared TiO_2–Ce_6-CpG, which not only effectively inhibited tumor growth, but also enhanced the function of the immune system, the mechanism of which mainly lies in the fact that TiO_2–Ce_6 can promote the effect of SDT and the immune response through CpG, an immune adjuvant. Furthermore, Yue *et al.*[34] utilized liposomes as a carrier to encapsulate the sound sensitizer hematoporphyrin monomethyl ether (HMME) and imiquimod (R837), an immune adjuvant, to prepare HMME/R837@Lip. Their study demonstrated that the combination of sono-sensitive nano-platforms and PD-L1 antibody significantly strengthened the anti-tumor effect, which markedly inhibited progression of the primary tumor and provided a long-term immune memory function to reduce tumor recurrence. Data in the current study were consistent with those in the above two reports.

In summary, this study demonstrated that PD-L1 Ab/Ce_6-NBs can target the specific tumor site, and the permeability of tumor endothelial cells can be enhanced by ultrasonic bursting of the NBs, thereby promoting the local enrichment of Ce_6 and PD-L1 Ab at the tumor. Simultaneously, Ce_6 generated a large amount of ROS through ultrasound irradiation to promote apoptosis and immunogenic death of hepatoma cells, ameliorating immune tolerance of the tumor microenvironment and boosting the effect of PD-L1 Ab on immunotherapy. The findings from this study showing the cooperation of the anti-tumor properties of ICIs and SDT provide a potential insight for the treatment of HCC.

Author contributions

Chaoqi Liu, Qing Zhou, and Yun Zhao conceived and designed the study. Chaoqi Liu, Yun Zhao, and Jun Zhou obtained the funding and provided laboratory support. Qing Zhou designed the methodology and coordinated responsibility for the research activity planning and execution. Yun Liu, Shiqi Yang, and Jinlin Li completed the main experiments and wrote the original draft of the manuscript. Yao Ma and Bing Hu provided software resources and performed data analysis. All authors contributed to writing and reviewing the manuscript.

Conflicts of interest

The authors have no conflicts of interest to declare.

Acknowledgements

The authors greatly appreciate the support from the Medical College of Three Gorges University and the Hubei Key Laboratory of the Tumor Microenvironment and Immunotherapy Foundation [Grant numbers 2018KZL02 and 2019KZL10]. And the research was also partially supported by the National Natural Science Foundation of China [Grant numbers 81673675].

References

1 L. Kulik and H. B. El-Serag, Epidemiology and management of hepatocellular carcinoma, *Gastroenterology*, 2019, **156**(2), 477–491.

2 A. Forner, M. Reig and J. Bruix, Hepatocellular carcinoma, *Lancet*, 2018, **391**(10127), 1301–1314.

3 A. Villanueva, Hepatocellular carcinoma, *N. Engl. J. Med.*, 2019, **380**(15), 1450–1462.

4 Z. Li, *et al.*, Expression and clinical significance of PD-1 in hepatocellular carcinoma tissues detected by a novel mouse anti-human PD-1 monoclonal antibody, *Internet J. Oncol.*, 2018, **52**(6), 2079–2092.

5 S. Kumagai, *et al.*, The PD-1 expression balance between effector and regulatory T cells predicts the clinical efficacy

of PD-1 blockade therapies, *Nat. Immunol.*, 2020, **21**(11), 1346–1358.

6 X. Wu, *et al.*, Application of PD-1 blockade in cancer immunotherapy, *Comput. Struct. Biotechnol. J.*, 2019, **17**, 661–674.

7 J. M. Llovet, *et al.*, Hepatocellular carcinoma, *Nature Reviews Disease Primers*, 2021, **7**(1), 6.

8 M. Meng, *et al.*, Doxorubicin nanobubble for combining ultrasonography and targeted chemotherapy of rabbit with VX2 liver tumor, *Tumour Immunobiol.*, 2016, **37**(7), 8673–8680.

9 W. Yue, *et al.*, Checkpoint blockade and nanosonosensitizer-augmented noninvasive sonodynamic therapy combination reduces tumour growth and metastases in mice, *Nat. Commun.*, 2019, **10**(1), 2025.

10 H. M. Zhu, *et al.*, Chlorin e6-loaded sonosensitive magnetic nanoliposomes conjugated with the magnetic field for enhancing anti-tumor effect of sonodynamic therapy, *Pharm. Dev. Technol.*, 2020, **25**(10), 1249–1259.

11 J. An, *et al.*, ROS-augmented and tumor-microenvironment responsive biodegradable nanoplatform for enhancing chemo-sonodynamic therapy, *Biomaterials*, 2020, **234**, 119761.

12 M. W. Teng, *et al.*, Classifying cancers based on T-cell infiltration and PD-L1, *Cancer Res.*, 2015, **75**(11), 2139–2145.

13 Y. Zhou, *et al.*, Targeted antiangiogenesis gene therapy using targeted cationic microbubbles conjugated with CD105 antibody compared with untargeted cationic and neutral microbubbles, *Theranostics*, 2015, **5**(4), 399–417.

14 Y. Tan, *et al.*, Nanobubbles containing sPD-1 and Ce6 mediate combination immunotherapy and suppress hepatocellular carcinoma in mice, *Int. J. Nanomed.*, 2021, **16**, 3241–3254.

15 J. Zeng, *et al.*, Chlorogenic acid ameliorates *Klebsiella pneumoniae*-induced pneumonia in immunosuppressed mice *via* inhibiting the activation of NLRP3 inflammasomes, *Food Funct.*, 2021, **12**(19), 9466–9475.

16 B. Farhood, M. Najafi and K. Mortezaee, CD8+ cytotoxic T lymphocytes in cancer immunotherapy: A review, *J. Cell. Physiol.*, 2019, **234**(6), 8509–8521.

17 V. P. Chauhan, *et al.*, Normalization of tumour blood vessels improves the delivery of nanomedicines in a size-dependent manner, *Nat. Nanotechnol.*, 2012, **7**, 383–388.

18 H. Li, *et al.*, Instant ultrasound-evoked precise nanobubble explosion and deep photodynamic therapy for tumors guided by molecular imaging, *ACS Appl. Mater. Interfaces*, 2021, **13**(18), 21097–21107.

19 X. Liu and S. Qin, Immune checkpoint inhibitors in hepatocellular carcinoma: Opportunities and challenges, *Oncologist*, 2019, **24**(1), S3–S10.

20 C. Wang, *et al.*, Tailoring biomaterials for cancer immunotherapy: Emerging trends and future outlook, *Adv. Mater.*, 2017, **29**(29), 1606036–1606060.

21 H. L. Liu, *et al.*, Focused ultrasound enhances central nervous system delivery of bevacizumab for malignant glioma treatment, *Radiology*, 2016, **281**(1), 99–108.

22 A. Ishijima, *et al.*, Selective intracellular vaporisation of antibody-conjugated phase-change nano-droplets *in vitro*, *Sci. Rep.*, 2017, **7**, 44077.

23 Y. T. Lee, Y. J. Tan and C. E. Oon, Molecular targeted therapy: Treating cancer with specificity, *Eur. J. Pharmacol.*, 2018, **834**, 188–196.

24 D. L. Ou, *et al.*, Development of a PD-L1-expressing orthotopic liver cancer model: Implications for immunotherapy for hepatocellular carcinoma, *Liver Cancer*, 2019, **8**(3), 155–171.

25 W. M. Becicka, *et al.*, The effect of PEGylation on the efficacy and uptake of an immunostimulatory nanoparticle in the tumor immune microenvironment, *Nanoscale Adv.*, 2021, **3**(17), 4961–4972.

26 H. Wang, *et al.*, Reprogramming tumor immune microenvironment (TIME) and metabolism *via* biomimetic targeting codelivery of Shikonin/JQ1, *Nano Lett.*, 2019, **19**(5), 2935–2944.

27 C. Liu, *et al.*, Treg cells promote the SREBP1-dependent metabolic fitness of tumor-promoting macrophages *via* repression of CD8+ T cell-derived interferon-γ, *Immunity*, 2019, **51**(2), 381–397.e6.

28 J. An, et al., ROS-augmented and tumor-microenvironment responsive biodegradable nanoplatform for enhancing chemo-sonodynamic therapy, *Biomaterials*, 2020, **234**, 119761.

29 Y. Wang, *et al.*, Immunogenic-cell-killing and immunosuppression-inhibiting nanomedicine, *Bioact. Mater.*, 2020, **6**(6), 1513–1527.

30 K. C. Mei, *et al.*, Liposomal delivery of mitoxantrone and a cholesteryl indoximod prodrug provides effective chemo-immunotherapy in multiple solid tumors, *ACS Nano*, 2020, **14**(10), 13343–13366.

31 J. W. Hodge, *et al.*, Chemotherapy-induced immunogenic modulation of tumor cells enhances killing by cytotoxic T lymphocytes and is distinct from immunogenic cell death, *Int. J. Cancer*, 2013, **133**(3), 624–636.

32 J. Lu, *et al.*, Nano-enabled pancreas cancer immunotherapy using immunogenic cell death and reversing immunosuppression, *Nat. Commun.*, 2017, **8**(1), 1811.

33 X. Lin, *et al.*, Nanosonosensitizer-augmented sonodynamic therapy combined with checkpoint blockade for cancer immunotherapy, *Int. J. Nanomed.*, 2021, **16**, 1889–1899.

34 W. Yue, *et al.*, Checkpoint blockade and nanosonosensitizer-augmented noninvasive sonodynamic therapy combination reduces tumour growth and metastases in mice, *Nat. Commun.*, 2019, **10**(1), 2025.